

## Energy landscape of small clusters of self-interstitial dumbbells in iron

M.-C. Marinica,<sup>1</sup> F. Willaime,<sup>1</sup> and N. Mousseau<sup>2</sup>

<sup>1</sup>CEA, DEN, Service de Recherches de Métallurgie Physique, F-91191 Gif-sur-Yvette, France

<sup>2</sup>Département de Physique and Regroupement Québécois Sur les Matériaux de Pointe, Université de Montréal, Case Postale 6128, Succursale Centre-ville, Montréal, Québec H3C 3J7, Canada

(Received 2 September 2010; revised manuscript received 15 January 2011; published 17 March 2011)

The activation-relaxation technique *nouveau* (ART<sub>n</sub>), a method for the systematic search of the minima and saddle-point configurations, is applied to the study of interstitial-cluster defects in iron. Some simple modifications to improve the efficiency of the ART<sub>n</sub> method for these types of applications are proposed. The energy landscapes at 0 K of defect clusters with up to four self-interstitial atoms obtained using the Ackland-Mendelev potential for iron are presented. The efficiency of the method is demonstrated in the case of monointerstitials. The number of different bound configurations increases very rapidly with cluster size from di- to quadri-interstitials. All these clusters can be analyzed as assemblies of dumbbells mostly with  $\langle 110 \rangle$  orientation. The lowest-energy configurations found with the present method and potential are made of parallel dumbbells. The mechanisms associated with the lowest saddle-point energies are analyzed. They include local rearrangements that do not contribute to long-range diffusion. The translation-rotation mechanism is confirmed for the migration of mono- and di-interstitials. For the tri-interstitial the migration is dominated by three mechanisms that do not involve the lowest-energy configuration. The migration of quadri-interstitials occurs by an on-site reorientation of the dumbbells in the  $\langle 111 \rangle$  direction, followed by the conventional easy glide. Finally, the minimum energy paths are investigated for the transformation toward the lowest-energy configuration of two specific clusters, including a quadri-interstitial cluster with a ring configuration, which was shown to exhibit an unexpected low mobility in previous molecular-dynamics simulations.

DOI: [10.1103/PhysRevB.83.094119](https://doi.org/10.1103/PhysRevB.83.094119)

PACS number(s): 68.43.Fg, 68.43.Hn, 68.43.Jk

### I. INTRODUCTION

The evolution of defects in materials is governed by events that range from nearly athermal to highly infrequent, i.e., with activation energies from meV to eV.<sup>1</sup> The atomistic simulation of such processes becomes even more challenging for irradiated materials owing to the increased diversity of lattice defects. In the past few years substantial efforts have been made to improve the efficiency in the simulation of such thermally activated events. Several finite-temperature methods have been proposed in the framework of molecular dynamics (MD): hyperdynamics,<sup>2</sup> parallel replica dynamics,<sup>3</sup> temperature accelerated dynamics,<sup>4</sup> action-derived molecular dynamics,<sup>5,6</sup> or properly obeying probability activation-relaxation technique (ART).<sup>7</sup> These methods, which provide recipes to accelerate the activated transition between local minima of the system at finite temperature, have proven to be very useful in radiation damage studies.<sup>8–11</sup> Other followed approaches are based on the reduction, at 0 K, of the energy landscape to the local minima configurations and the first-order saddle points that link them. This information is sufficient, away from melting, to fully determine the system's thermodynamics and kinetics using transition-state theory within, for example, the quasiharmonic approximation.

Algorithms for finding saddle points at 0 K can be divided into two classes: (i) the ones based on an interpolation between two known minima and (ii) those using only local information around a given minimum. In the first class, an initial diffusion pathway is first constructed and then optimized thanks to algorithms such as the nudged elastic band (NEB) method.<sup>12,13</sup> A review of such methods can be found in Refs. 14 and 15. Algorithms for the second class are more complex because they

combine uphill climbs to escape from the minimum and relaxations in the perpendicular direction to find valleys bringing to saddle points. The saddle point is generally found by following the eigenvector corresponding to the lowest eigenvalue of the Hessian. The efficiency of the initial algorithms<sup>15–18</sup> has been recently improved mainly by replacing the calculation of the full Hessian matrix and its spectrum—which is a prohibitive task for large systems—by that of only the lowest eigenvalue and corresponding eigenvector. This includes the ART<sup>19</sup> or ART *nouveau* (ART<sub>n</sub>),<sup>20–22</sup> and the dimer<sup>18,23</sup> and the hybrid eigenvector-following methods.<sup>15,24</sup>

Interstitial-type defects formed by the clustering of self-interstitials produced under irradiation have rather peculiar properties in  $\alpha$ -iron in comparison with other bcc metals, where all interstitial-type defects are predominantly  $\langle 111 \rangle$ . In  $\alpha$ -iron, isolated self-interstitial atoms (SIAs) have a rather large migration energy,  $\sim 0.3$  eV,<sup>25</sup> instead of tens of meV in other bcc metals. Density-functional theory (DFT) calculations<sup>26–28</sup> show that in bcc Fe, the  $\langle 110 \rangle$  dumbbell configuration is adopted while in all the other bcc transition metals the  $\langle 111 \rangle$  crowdion configuration has the lowest formation energy.<sup>29</sup> Nanometer size clusters—or dislocation loops—have either  $\langle 111 \rangle$  or  $\langle 100 \rangle$  orientation in Fe.<sup>30–32</sup> The structure of interstitial clusters with an intermediate size is largely unknown, although they play a key role in the loop growth mechanism.<sup>31,33,34</sup> The  $\langle 111 \rangle$  loops can glide very easily, as observed in MD simulations,<sup>33–35</sup> with an activation energy lower than 0.1 eV, whereas the  $\langle 100 \rangle$  loops are very weakly mobile, with an estimated activation energy larger than 2.5 eV.<sup>33</sup> The competition between these various orientations raises the question of their relative stabilities as functions of cluster size and temperature. Dudarev *et al.* indeed

predicted that the  $\langle 100 \rangle$  orientation should be favored at high temperatures based on the magnetism-driven reduction of the  $C'$  elastic constant.<sup>36</sup>

*Ab initio* calculations, as well as empirical potentials, account for the stability of  $\langle 110 \rangle$  dumbbells,<sup>26–28</sup> and they predict that the transition from  $\langle 110 \rangle$  to  $\langle 111 \rangle$  orientation occurs typically at approximately five SIAs.<sup>28,37</sup> The purpose of the present paper is to investigate more deeply the properties of SIA clusters with two to four defects. Their structure and mobility are extremely important for the kinetic evolution of iron-based materials and they clearly need to be further investigated. Two types of studies have been performed so far in this direction. The first consists in letting the system evolve by standard MD simulations with after-the-fact reconstruction of diffusion events. However, because rather high activation energies are involved, quite high temperatures, namely, up to 1200 K, are required to explore the energy landscape.<sup>35,38</sup> As a consequence, it is difficult to identify the observed structures and migration mechanisms that are relevant at lower temperatures, such as reactor pressure vessel steel operating temperatures,  $\sim 550$  K, or temperatures at which defect characterization experiments such as resistivity recovery measurements are performed (100–400 K).<sup>39</sup> Moreover, on the MD time scale (a few ns) the system can be trapped easily in small regions of the phase space. The second type of investigation is based on the energy evaluation of a series of defect configurations and migration pathways at 0 K. Until now, however, these configurations were typically chosen based on intuition and were normally restricted to configurations made of parallel dumbbells. The limitation of this approach was illustrated recently by the fact that unguessed low-energy configurations made of nonparallel dumbbells were evidenced using high-temperature MD simulations.<sup>34</sup> However, these configurations could be observed in MD simulations only because they have large formation entropies and hence dramatically reduced free energies at high temperature. Therefore, one cannot exclude the existence of other important nonconventional configurations or migration mechanism characteristics of low temperature that cannot be observed in high-temperature MD simulations. It was indeed shown by quasiharmonic calculations that finite-temperature effects play an important role in these defects, because, for instance, low-frequency modes tend to stabilize  $\langle 111 \rangle$  configurations over  $\langle 110 \rangle$  ones at high temperatures.<sup>40</sup>

The goal of the present paper is to investigate the low-temperature properties of small SIA clusters in Fe using the ART $n$  approach in order to cope with the limitations, on the one hand, of the high-temperature MD simulations and, on the other hand, of the intuition-based selection of configurations. As in the MD studies by Terentyev *et al.*<sup>35</sup> and Anento *et al.*,<sup>38</sup> the present work is based the Ackland-Mendelev embedded atom method (EAM) potential for iron developed in Ref. 41. It corresponds to an improved version of the potential 2 developed by Mendelev *et al.*<sup>42</sup> These potentials were shown to perform quite well for point defects and point defect clusters, when compared to *ab initio* calculations,<sup>28</sup> although one must bear in mind that some limitations have been pointed out concerning in particular the relative stability of some nonparallel configurations.<sup>34</sup>

The paper is organized as follows. Section II gives a brief presentation of the ART $n$  method, completed by Appendixes A and B. The energy landscapes for interstitial defects containing from one to four SIAs—denoted respectively,  $I$ ,  $I_2$ ,  $I_3$ , and  $I_4$ —are presented in Sec. III. In the last part of Sec. III the transition pathways from ring configurations of  $I_3$  and  $I_4$  to the lowest-energy configurations are investigated.

## II. METHODOLOGY

### A. ART nouveau (activation-relaxation technique)

The ART $n$  method is designed to explore the energy landscape of the system using only the local information, namely, the lowest eigenvalue and eigenvector of the Hessian, according to a two-step process: activation and relaxation.

(1) *The activation.* Starting from the  $i$ th explored local minimum, with coordinates  $\mathbf{q}^{i0}$ , the  $i$ th saddle point, with coordinates  $\mathbf{q}^{is}$ , is searched for as follows.

(a) A random direction of deformation,  $\delta\mathbf{q}^i$ , is chosen, and the system is slowly pushed in this direction. The idea is to go uphill in this direction until reaching the inflexion point of the energy surface. Successive images of the system are constructed according to

$$\mathbf{q}_k^i = \mathbf{q}_{k-1}^i + \frac{\delta x_A}{\|\delta\mathbf{q}^i\|} \delta\mathbf{q}^i. \quad (1)$$

The choices of displacement amplitude between images,  $\delta x_A$ , and random deformation,  $\delta\mathbf{q}^i$ , are discussed in Appendix A. At each step,  $k$ , before constructing the next image, the system is relaxed in the hyperplane orthogonal to  $\delta\mathbf{q}^i$  using damped MD after which the lowest eigenvalue of the Hessian  $\lambda_1$  is computed. If  $\lambda_1$  is positive, the deformation is increased one step further. If  $\lambda_1$  is negative, or more precisely, if it becomes lower than a negative threshold value, which is set at  $\lambda_c = -0.5$  eV/Å for the present study, the procedure described below is applied. For a typical value of  $\delta x_A = 0.6$  Å only four to six steps are needed before  $\lambda_1 \leq \lambda_c$ .

(b) Once  $\lambda_1$  is negative, the convergence to the saddle point is achieved by going along the eigenvector corresponding to this lowest eigenvalue  $\mathbf{v}_1$ :

$$\mathbf{q}_n^i = \mathbf{q}_{n-1}^i - \frac{\delta x_a^n}{\|\mathbf{v}_1\|} \mathbf{v}_1. \quad (2)$$

The displacement amplitude between images ( $n-1$ ) and  $n$ ,  $\delta x_a^n$ , needs to become smaller as the saddle point is approached; it is chosen as  $\delta x_a^n = \delta x_a / n^{1/2}$ , where  $\delta x_a$  is smaller than  $\delta x_A$  to ensure convergence to the saddle point. In this paper we have used a ratio  $\delta x_a / \delta x_A = 0.4$ . The average number of activation steps is  $n \sim 20$ . We have tested several values of  $\delta x_a$  without noticing major differences. Note that in more difficult cases, it could be useful to update  $\delta x_a^n$  using the adaptative method proposed by Wales *et al.*<sup>15,24</sup> in the hybrid eigenvector-following method and by Cancès *et al.*<sup>43</sup> in ART $n$ . As in the previous step, each configuration  $\mathbf{q}_n^i$  is relaxed in the hyperplane orthogonal to  $\mathbf{v}_1$ . If the lowest eigenvalue becomes positive, procedure 1(a) is started again from configuration  $\mathbf{q}^{i0}$  with a new random direction  $\delta\mathbf{q}^i$ .

(2) *The relaxation.* This straightforward step consists in relaxing the system into the local minimum,  $\mathbf{q}^{(i+1)0}$ , on the other side of the saddle point. It can be achieved with

any standard minimization technique. We have used, again, damped MD; i.e., the system is propagated with the Verlet algorithm with a time step of 7 fs. Before applying this algorithm, however, the configuration is normally pushed slightly over the saddle point, away from the initial minimum, to ensure that the relaxation will lead to a new local minimum. The relaxation is considered to be achieved when all forces are smaller than  $10^{-4}$  eV/Å.

One of the central points of the ART $n$  method is that the evaluation of  $\lambda_1$  and  $\mathbf{v}_1$  is performed using the Lanczos method. Its implementation in ART $n$  and the proofs of convergence with a basis set size  $l = 15$  used here are presented in Appendix A.

### B. Efficiency

The most important criterion to measure the efficiency of the ART $n$  method is the total number of force evaluations per successful saddle-point search. In some systems, this number may depend weakly on the system size, as shown by Olsen *et al.*<sup>17</sup> using the dimer or ART methods for surface systems. For large cells, Mousseau *et al.*<sup>20,21</sup> noted that it is preferable to use a local initial deformation instead of a global one to prevent the simultaneous initiation of independent local basin escape trajectories in different parts of the cell. From the analysis of the results in Appendix A, we conclude that the local deformation, centered on the defect, is indeed the most efficient method. With this type of deformation, the number of force evaluations is independent on the size of the system.

### C. Analysis of the ART $n$ trajectories

Unless otherwise stated, the size of the system is  $8a_0 \times 8a_0 \times 8a_0$ , where  $a_0$  is the lattice parameter, i.e., 1024 lattice sites. The statistic is made over 50 trajectories, which are stopped after 2000 successful activation events. Each simulation is started from the configuration with the lowest known energy. With aggressive parameters, the system can climb very high in energy during the activation process and the saddle point that is found may not be directly connected to the starting minimum. This is, for instance, obviously the case when the saddle-point energy is lower than the starting point energy. More generally, nudged elastic band calculations were therefore performed between all initial and final configurations in order to exclude events between minima that are not directly connected. This procedure is not necessary if a small activation step is chosen, e.g.,  $\delta x_A = 0.005$  Å. However, as explained in Appendix A, for efficiency reasons,  $\delta x_A = 0.6$  Å is used here.

The output of an ART $n$  simulation is a set of three configurations minimum- saddle point-minimum which is called event. This information can serve first to identify low-energy configurations but also low-energy pathways that are important for the kinetic evolution of the system. Our aim is to explore states corresponding to clustered interstitials, and not states made by separated defects, e.g., a  $I_{n-1}$  cluster and a self-interstitial. The difficulty is that these states are not very far in energy from the lowest-energy configuration, because the binding energy between  $I$  and  $I_{n-1}$  is of the order of 1 eV. For this reason, the phase-space exploration is performed using a Metropolis algorithm and a fictitious temperature. In

other words, the starting configuration for the next saddle-point search is the new minimum if its energy is lower than that of the previous minimum, or otherwise either of the two minima with a probability proportional to their Boltzmann weights. This favors low-energy configurations without systematically rejecting the configuration that increase the energy. The value of the fictitious temperature is a key parameter of the method. If it is too high, most of the time is spent exploring dissociated configurations. If it is too low, it could be the case that the simulation misses clustered configurations belonging to an energy basin separated from the initial one by a high-energy saddle point. As a compromise, the fictitious temperature is set to 1200 K in the present study. For the same reason, if the current configuration has an energy 2 eV higher than the lowest-energy configuration, it is replaced with the initial configuration.

The interstitial atoms are localized using the Wigner-Seitz method.<sup>35</sup> Two configurations are considered as nonequivalent if their energies differ by more than  $10^{-2}$  eV and if the sum of squares of the principal components of the inertia tensor of the interstitial atoms are different.

The histograms of the energy distribution for a given cluster size are plotted with 0.01 eV intervals. We denote by  $I_n^{(hkl)}$  the lowest-energy  $I_n$  cluster formed by  $n$  parallel dumbbells aligned along the  $\langle hkl \rangle$  direction. A few other specific configurations are discussed. They are labeled  $I_n^m$ , where  $m$  denotes the energy interval (1,2,3, ...). When more than one configuration is present in the interval, a letter ( $a, b, c, \dots$ ) is added in the superscript.

## III. RESULTS

### A. Monointerstitials

The case of the monointerstitials is quite simple and it has already been investigated in depth in several local minimization studies.<sup>27,28</sup> This section can therefore be considered as a validation of the present methodology, i.e., to make sure that all the configurations and migration pathways that have been proposed are found, but in an automatic way.

The histogram of all the configurations found after  $10^5$  successful ART $n$  events is shown in Fig. 1. In this particular case, it is actually sufficient to compute only a few hundred events. In agreement with previous static calculations, the  $I_1^{(110)}$  dumbbell is the most stable configuration, with a formation energy of 3.52 eV. It is followed, 0.42–0.43 eV higher in energy, by a set of configurations close to the  $\langle 111 \rangle$  dumbbell. This includes a dumbbell that is slightly tilted toward the  $\langle 110 \rangle$  direction, with a tilt angle  $\approx 9.9^\circ$ . It will therefore be denoted  $\langle 11\xi \rangle$  in the following. It also includes the so-called crowdion configuration, which is obtained by placing one extra atom in between two nearest neighbors in the  $\langle 111 \rangle$  dense direction. Finally, 0.61 and 0.64 eV higher are the tetrahedral ( $I_1^{\text{tet}}$ ) and octahedral ( $I_1^{\text{oct}}$ ) configurations, respectively. In DFT calculations with cells with up to 251 atoms, the  $\langle 100 \rangle$  dumbbell was also found to be a local minimum. This configuration is also metastable with the Ackland-Mendelev potential for small cell sizes.<sup>28</sup> It is not found here because it decays into the octahedral configuration for cells with 1024 atoms or more. Note that the  $\langle 100 \rangle$

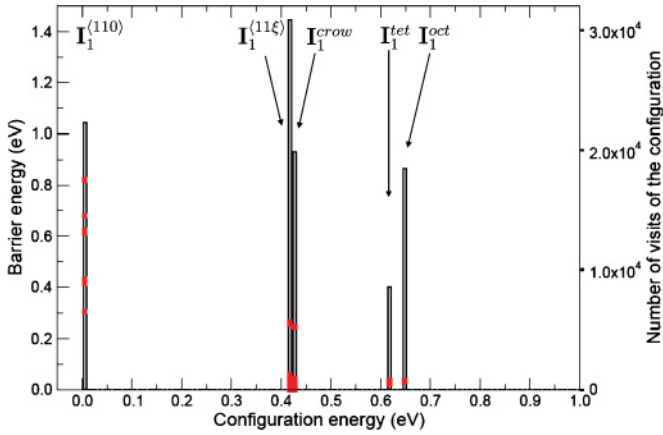


FIG. 1. (Color online) Histogram of the relative formation energies and their associated barrier energies for ART $n$ -generated events of the monointerstitial in iron modeled by the Ackland-Mendelev potential. The origin of the abscissa is the energy of the most stable configuration, the  $I_1^{(110)}$  dumbbell. The black bars, associated with the vertical axis on the right-hand side, correspond to the occurrence of the configurations in the  $10^5$  event ART $n$  trajectory. The red squares represent the barrier energies of the saddle points linked to the corresponding configuration. The barrier energy is the difference between the saddle-point energy and the energy of the corresponding local minima configuration. For  $I_1^{(110)}$ , the exact values to each barrier energy of the migration and on-site rotation mechanisms are reported in Table I.

dumbbell is unlikely to decay to the octahedral configuration at large cell sizes within DFT, because the DFT formation energy of the octahedral configuration is larger than that of the  $\langle 100 \rangle$  dumbbell, at variance with the Ackland-Mendelev potential behavior. This discrepancy comes from the fact that the *ab initio* formation energies of the octahedral and tetrahedral configurations were not used in the fit of the Ackland-Mendelev potential.

For each configuration, the set of energy barriers found to escape from the local minimum are also plotted in Fig. 1. All the barriers that have been proposed from static calculations starting from the  $\langle 110 \rangle$  ground-state configuration are also found here and summarized in the Table I. The lowest barrier at 0.31 eV corresponds to the nearest-neighbor translation-

rotation migration mechanism proposed by Johnson.<sup>44</sup> The next two barriers correspond to the on-site reorientation into an equivalent  $\langle 110 \rangle$  dumbbell and the  $\langle 11\xi \rangle$  dumbbell, respectively. Then come the migrations toward the nearest neighbor by the translation mechanism, the second nearest-neighbor  $\langle 110 \rangle$  dumbbell, and the tetrahedral and octahedral configurations. The latter two were not investigated before. And finally comes the third nearest-neighbor jump.

In order to test the accuracy of the energy barriers found in the ART $n$  simulations, we have recalculated them using two-ended methods. We used both the drag method<sup>27,28</sup> and the NEB method.<sup>12,13</sup> The results are found to be the same for the three methods within, at most, 0.01 eV. This is also the case when using smaller cell sizes (129 atoms). The results are summarized in Table I.

Regarding the  $I_1^{(11\xi)}$  configuration, the small barriers correspond to the migration of the dumbbell in the  $\langle 111 \rangle$  direction or to the reorientation of the dumbbell into the  $\langle 110 \rangle$  direction. It is interesting to note that ART $n$  also finds some paths to the tetrahedral and octahedral configurations, with barriers of 0.25 eV.

From this analysis it is clear that the most important mechanism in the monointerstitial migration for this potential is the Johnson mechanism with a 0.31 eV activation energy. The dumbbell can migrate to four nearest-neighbor sites and for each of them it can adopt two final orientations. As a result its motion is three dimensional (3D). Indeed, using MD and the same potential, Terentyev *et al.*<sup>35</sup> and Anento *et al.*<sup>38</sup> found that the migration path for the single SIA is fully 3D in the 300–1000 K range. Using a simple Arrhenius interpolation from 400 to 1000 K, Terentyev *et al.*<sup>35</sup> estimated the effective migration barrier to be 0.31 eV.<sup>35</sup> Thanks to better statistics, Anento *et al.*<sup>38</sup> were able to show that the Arrhenius curve of the diffusion coefficient is in fact curved, with a slope of 0.30 eV below 500 K and 0.20 eV at higher temperatures. The low-temperatures results are in perfect agreement with the present 0 K calculations.

Terentyev *et al.*<sup>35</sup> observed that the single SIA reorients from the  $\langle 110 \rangle \rightarrow \langle 11\xi \rangle$  configuration at high temperature, with an effective reorientation energy of 0.69 eV. The discrepancy with the present static calculation, 0.43 eV, can be owing either to finite-temperature effects or to the fact that the MD error bars are quite large for this infrequent event.

## B. Di-interstitials

The energy distribution of all the configurations found by ART $n$  at 0 K starting from a di-interstitial made of nearest-neighbor parallel  $\langle 110 \rangle$  dumbbells is represented in Fig. 2. The lowest-energy configuration found with the present potential is the nearest-neighbor parallel dumbbell,  $I_2^{(110)}$ , with a formation energy of 6.21 eV, i.e., a binding energy of 0.83 eV. There are more than 200 distinct bound configurations, i.e., with an energy strictly lower than that of two isolated  $\langle 110 \rangle$  dumbbells. However, *only* 80 of them are below 0.76 eV. More generally, the broad peak at  $\sim 0.83$  eV contains hundreds of configurations of two  $\langle 110 \rangle$  separated dumbbells at various distances and with various orientations. Only a small set of the bound configurations is made of parallel dumbbells. Among them, the first parallel metastable state, with an excess energy of 0.48 eV,

TABLE I. Calculated migration and on-site rotation energies of the  $\langle 110 \rangle$  monointerstitial obtained using ART $n$  with two supercell sizes: 129 and 1025 atoms. For the schematic representation of the  $I_1^{(110)} \rightarrow I_1^{(110)}$  mechanisms, see Ref. 27.

Mechanism	Size	
	129	1025
NN translation-rotation	0.31	0.31
[110]-[011]	0.43	0.41
[110]-[11 $\xi$ ]	0.43	0.43
NN translation	0.46	0.43
Second NN	0.62	0.61
[110]-tetrahedral	0.64	0.62
[110]-octahedral	0.69	0.68
Third NN	0.87	0.83

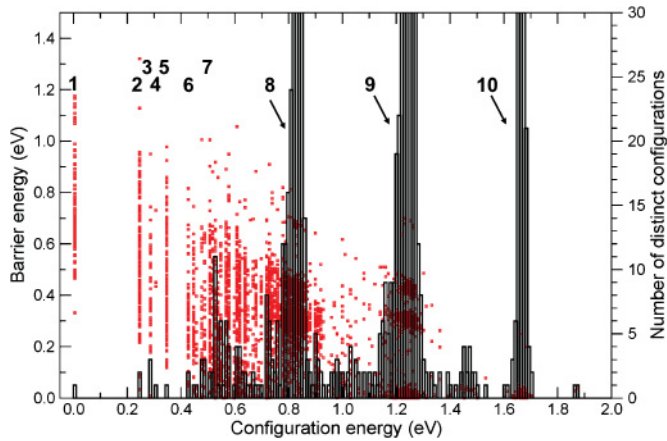


FIG. 2. (Color online) Histogram of the relative formation energies and associated barrier energies (red squares and left vertical axis) of the ART $n$ -generated configurations for di-interstitials in iron modeled by the Ackland-Mendelev potential. The configuration energies are taken with respect to the  $I_2^{(110)}$  configuration. The vertical axis on the right-hand side (associated with the bars) corresponds to the number of distinct minima found by ART $n$ . Labels 1–5 denote energy intervals with low-energy configurations. The quasicontinuum of states starts at label 6. Label 7 corresponds to interval containing the parallel configurations ( $I_2^{(111)}$ ), and finally labels 8, 9, and 10 represent states with two separated dumbbells, oriented, respectively, both along  $\langle 110 \rangle$ , one along  $\langle 110 \rangle$  and the other along  $\langle 111 \rangle$ , and both along  $\langle 111 \rangle$ . The peaks labeled 8, 9, and 10 are truncated on the figure, and their maxima are 74, 211, and 55, respectively.

is the nearest-neighbor  $I_2^{(100)}$  dumbbell configuration. With an excess energy 0.53 eV,  $I_2^{(111)}$  is made of two parallel  $\langle 111 \rangle$  dumbbells at first- or second-nearest-neighbor distance; these two configurations are nearly degenerate in energy. Between the two lowest-energy configurations with parallel dumbbells,  $I_2^{(110)}$  (interval 1) and  $I_2^{(100)}$ , there are several nonparallel configurations. The configurations, associated with the six filled lowest-energy intervals, are represented in Fig. 3.

The  $I_2^{2a}$  configuration is formed by two dumbbells at third-nearest-neighbor distance,  $a_0\sqrt{2}$ : One is aligned along  $[1-10]$  and the other one is aligned along  $[01-1]$ . This configuration is important as it can be formed from  $I_2^{(110)}$  by a Johnson jump (see the discussion of Fig. 5 below), and it corresponds to the intermediate configuration for the two-step migration mechanism of  $I_2$ .<sup>27</sup> The  $I_2^{2b}$ ,  $I_2^{3a}$ ,  $I_2^{3b}$ ,  $I_2^{3c}$ , and  $I_2^{4a}$  configurations belong to the same class of defects. Let us start with the  $I_2^{3b}$ , which can be seen as three  $\langle 110 \rangle$  dumbbells and one vacancy. This configuration was reported first by Gao *et al.*<sup>45</sup> from MD simulations of a displacement cascade using another potential, and it was observed recently to form spontaneously from  $\langle 110 \rangle$  dumbbells in MD simulations using the Ackland-Mendelev potential.<sup>34</sup> This configuration is very close in geometry to either two nearest-neighbor perpendicular  $\langle 110 \rangle$  dumbbells (configuration  $I_2^{2b}$ ) or two third-nearest-neighbor nonparallel dumbbells (configuration  $I_2^{3a}$ ). These two configurations are local minima for the present potential, as well as their respective two slightly tilted analogs,  $I_2^4$  and  $I_2^{3c}$ . Note that the  $I_2^{3b}$  configuration was found to have an energy even lower than that of  $I_2^{(110)}$  in DFT calculations.<sup>34</sup>

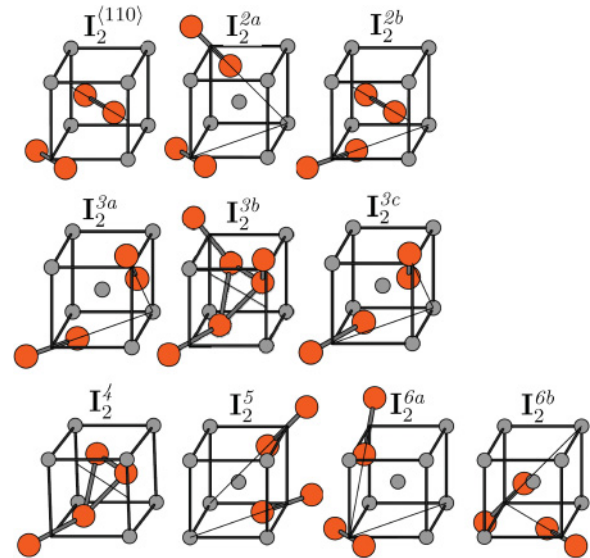


FIG. 3. (Color online) Schematic representation of the lowest-energy configurations (below the quasicontinuum) of the di-interstitial.

This may have consequences on the mobility of  $I_2$  because no straightforward mechanism exists for the migration of this configuration. Because this type of defect was first observed by Gao *et al.*,<sup>45</sup> it will be referred to as a Gao-type defect in the following.

Configurations  $I_2^5$ ,  $I_2^{6a}$ , and  $I_2^{6b}$  are other second- or third-nearest-neighbor configurations of nonparallel  $\langle 110 \rangle$  dumbbells (see Fig. 3). Above 0.42 eV (interval 6) the distribution of states becomes quasicontinuous. For energies higher than the binding energy, namely, 0.83 eV, the configurations found by ART $n$  are not relevant for di-interstitials, because they are made of two separated self-interstitials. However, the energy spectrum is interesting because it reveals the capacity of ART $n$  to capture the three families of pairs of stable or metastable self-interstitial configurations. As discussed above, the broad peak at 0.83 eV, labeled 8 in Fig. 2, is populated by configurations made of two  $I_1^{(110)}$  dumbbells. Similarly, the broad peaks labeled 9 and 10 correspond to separated dumbbells, the first one being  $I_1^{(111)}$  and the second one being, respectively,  $I_1^{(110)}$  and  $I_1^{(111)}$ .

The spectrum of energy barriers is also quasicontinuous. However, not all barriers are important for long-range diffusion: The small barriers (in the meV range) often correspond to a transition from high-energy configurations to the lower-energy configurations, e.g., from  $I_2^{(111)}$  to  $I_2^{(110)}$ . What is more relevant for the migration behavior is the saddle-point energy, i.e., the energy difference of the saddle point with respect to the ground-state configuration and not with respect to the initial configuration of the jump. As shown in Fig. 4, the three lowest saddle-point energies  $E_{s,2}^{\alpha\beta\gamma}$  are 0.28, 0.33, and 0.47 eV. The corresponding mechanisms are represented in Fig. 5. The lowest saddle-point energy ones,  $E_{s,2}^{\alpha} = 0.28$  eV, do not contribute to the migration. They indeed correspond (1) to simultaneous double Johnson jumps between two  $I_2^{2b}$  configurations, (2) to small local reorientations between  $I_2^{2b}$  and  $I_2^{3a}$  configurations, where the barrier is



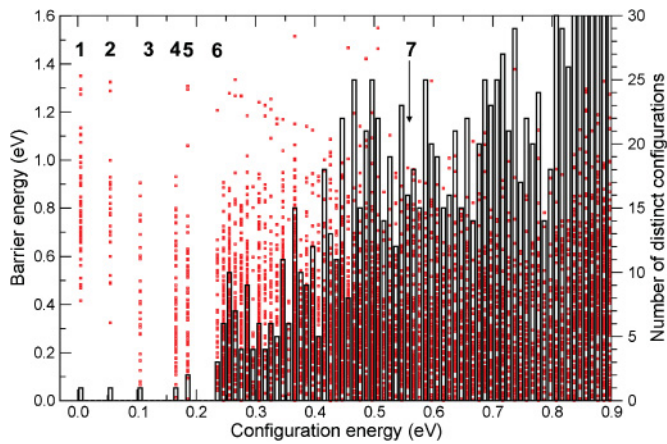


FIG. 6. (Color online) Histogram of the relative formation energies and associated barrier energies of ART $n$ -generated configurations for  $I_3$ . The same convention as in Fig. 2 is applied. The zero energy of the abscissa corresponds to the most stable configuration,  $I_3^{(110)}$ . Labels 1–6 denote the first states before the quasicontinuum; the corresponding configurations are illustrated in Fig. 7. Label 7 corresponds to the  $\langle 111 \rangle$  parallel configuration,  $I_3^{(111)}$ .

added to a Gao-type defect, respectively,  $I_2^{2b}$  and  $I_2^{3b}$ . More than 1000 distinct bound configurations were found for  $I_3$ , as illustrated in Fig. 6. As in the case of  $I_2$  there are many nonparallel configurations between  $I_3^{(110)}$  and the first  $\langle 111 \rangle$  parallel configuration,  $I_3^{(111)}$ , which lies at 0.54 eV.

The barriers associated with  $I_3^{(110)}$  are more complex than for  $I_2^{(110)}$  and  $I_2^{(110)}$ . First, performing the same Johnson translation-rotation jumps for the three dumbbells yields a configuration with parallel dumbbells, an energy of 0.41 eV, which is obviously different from  $I_3^{(110)}$ , and a barrier height of

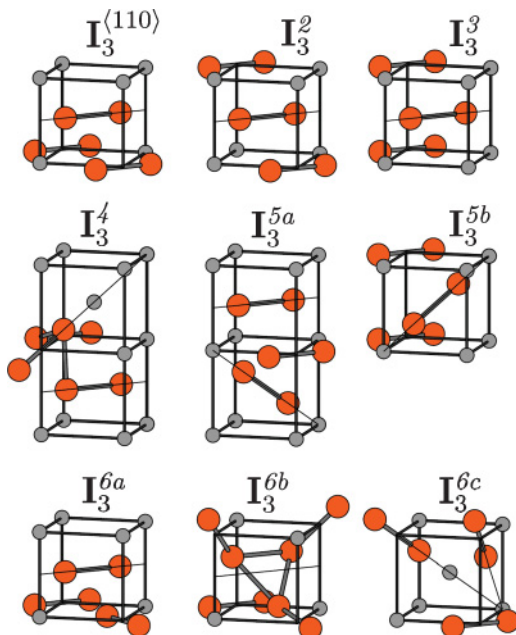


FIG. 7. (Color online) Schematic representation of the tri-interstitial configurations below the quasicontinuum from Fig. 6. The same convention as in Fig. 3 is used.

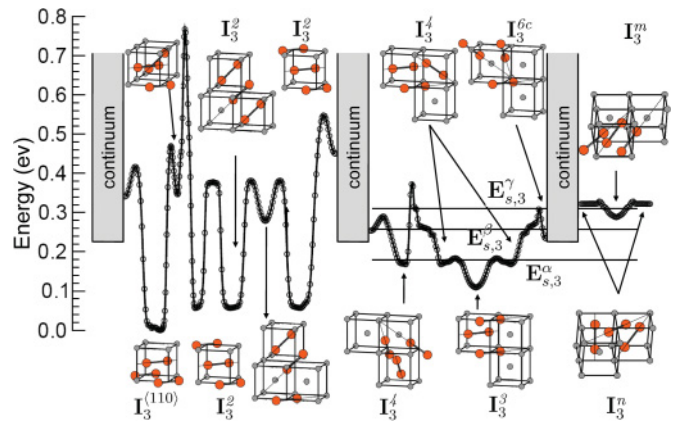


FIG. 8. (Color online) Schematic representation of three energy basins of the energy landscape of tri-interstitials. The first two basins involve low-energy configurations and the third one involves mixed configurations composed of  $\langle 111 \rangle$  and  $\langle 110 \rangle$  dumbbells,  $I_3^m$  and  $I_3^n$ . The lowest saddle-point energies,  $E_{s,3}^{\alpha,\beta,\gamma}$ , from Fig. 4 are also represented.

0.62 eV. No combination of two or three jumps transforming an  $I_3^{(110)}$  state into another  $I_3^{(110)}$  configuration could be found. The two lowest-energy barriers of  $I_3^{(110)}$  are illustrated in Fig. 8. They correspond to the jump of only one SIA by the Johnson mechanism. The lowest one is 0.42 eV high and it connects to a configuration at 0.34 eV, which is already in the continuum of states. The second highest barrier, at 0.46 eV, yields a configuration which is an intermediate state for the transformation into  $I_3^2$  (see Fig. 8). The activation energy for the  $I_3^{(110)}$ -to- $I_3^2$  transformation is 0.78 eV. Unlike  $I_3^{(110)}$ ,  $I_3^2$  can migrate with the Johnson mechanism with the same barrier energy as  $I_2^{(110)}$ , i.e., 0.33 eV. Note that ART $n$  and NEB provide the same value but that the barrier obtained with the drag method is 0.48 eV.

The situation in the energy basin around  $I_3^3$  is quite interesting. First,  $I_3^3$  can easily transform into  $I_3^4$ , by a nearest-neighbor translation-rotation jump of one of the  $\langle 110 \rangle$  dumbbells to a  $\langle 111 \rangle$  dumbbell, with a barrier energy of 0.08 eV (see Fig. 8). More generally, configurations  $I_3^3$ ,  $I_3^4$ ,  $I_3^{5a}$ ,  $I_3^{5b}$ ,  $I_3^{6a}$ ,  $I_3^{6b}$ , and  $I_3^{6c}$  (see Fig. 7) are connected by rather low-energy barriers. For instance, the barriers for  $I_3^3 \rightarrow I_3^{5a}$ ,  $I_3^{5a} \rightarrow I_3^{6a}$ , and  $I_3^4 \rightarrow I_3^{6c}$  are, respectively, 0.11, 0.13, and 0.17 eV. The last one is illustrated in Fig. 8. All these barriers correspond to local rearrangements, which do not yield any long-range diffusion. However,  $I_3^4$  can migrate as a unit in the  $\langle 111 \rangle$  direction by a low-energy mechanism, namely, 0.20 eV. This mechanism, illustrated in Fig. 8, consists of two simultaneous Johnson jumps of the  $\langle 110 \rangle$  dumbbells, and a glide of the  $\langle 111 \rangle$  dumbbell. The saddle-point energy of this mechanism, 0.36 eV, is almost the same as that of the migration of  $I_3^2$  by the Johnson mechanism (0.38 eV).

Finally, an analysis of the ART $n$  trajectories revealed that the lowest saddle-point energy migration mechanism (0.33 eV) is associated with a configuration in the continuum of states, i.e., with an energy of 0.29 eV, which can migrate with a very low barrier (35 meV). This configuration, denoted  $I_3^m$ , is made of two  $\langle 111 \rangle$  dumbbells and one  $\langle 110 \rangle$  dumbbell.

The migration mechanism, illustrated in Fig. 8, involves an intermediate configuration with an energy of 0.32 eV,  $I_3^n$ , with two nonparallel  $\langle 110 \rangle$  dumbbells and one  $\langle 111 \rangle$  dumbbell. This mechanism involves a pure translation of one of the  $\langle 111 \rangle$  dumbbells and nearest-neighbor translation-rotation jumps of the other dumbbells.

In summary, the energy landscape of tri-interstitials can be schematized as follows. There is no simple mechanism that brings the lowest-energy configuration,  $I_3^{(110)}$ , into an equivalent configuration. On the other hand, three energy basins with migration mechanisms having a saddle-point energy in the range 0.33–0.38 eV have been identified. The first one involves the  $I_3^2$  configuration, which can migrate by simultaneous or successive Johnson jumps of the aligned and parallel  $\langle 110 \rangle$  dumbbells. A two-jump transformation linking  $I_3^{(110)}$  to  $I_3^2$  with a barrier of 0.78 eV has been found. The second basin involves the seven other configurations before the continuum of states. These configurations are linked by low-energy barriers and they can migrate by first transforming to  $I_3^4$ , which can jump into a nearest neighbor  $I_3^4$ . The third basin involves an even higher-energy minimum (0.30 eV) corresponding to a mixed  $\langle 110 \rangle$ - $\langle 111 \rangle$  configuration, which can glide easily in the  $\langle 111 \rangle$  direction via another mixed configuration. The saddle points with lower energies (Fig. 4) correspond to local rearrangements that do not yield any long-range diffusion; for instance,  $E_{s,3}^\alpha$ , at 0.18 eV, corresponds to the saddle point between  $I_3^3$  and  $I_3^4$ .

Using MD and the same potential, Anento *et al.*<sup>38</sup> observed that during diffusion the tri-interstitial goes through several configurations, which include  $\langle 110 \rangle$  and  $\langle 111 \rangle$  dumbbells, in agreement with the present energy landscape. They describe the migration process as  $\langle 111 \rangle$  one-dimensional (1D) glides with occasional rotations to more stable  $\langle 110 \rangle$  configurations. They report activation energies for diffusion and rotation ranging from 0.1 to 0.16 eV. On the other hand, Terentyev *et al.*<sup>35</sup> found that below 600 K the migration of the tri-interstitial is fully 3D and that at higher temperatures it includes  $\langle 111 \rangle$  glides with an effective migration energy of 0.16 eV. The present energy landscape is more compatible with the latter analysis, considering that migration is dominated by the 2D-3D mechanisms from the first two basins at low temperature and by the 1D mechanism of the third basin at high temperature. It is indeed very likely that the excess vibrational entropy of  $\langle 111 \rangle$  dumbbells<sup>40</sup> stabilizes the configurations of the third basin,  $I_3^m$  and  $I_3^n$ , at high temperature. In order to make a closer and more quantitative comparison, it is necessary, on the one hand, to better analyze the low-temperature MD configurations, and, on the other hand, to perform kinetic Monte Carlo (kMC) type simulations on the present energy landscape.

#### D. Tetra-interstitials

The same ARTn simulations performed for  $I_4$  yield an even larger number of configurations (Fig. 9), with more than 1500 distinct bound configurations. The lowest-energy configuration is made of  $\langle \zeta \zeta 0 \rangle$  parallel dumbbells that are slightly tilted from  $\langle 110 \rangle$  (see Fig. 10). It has a formation energy of 10.94 eV and hence the binding energy between  $I_3^{(110)}$  and  $I_1^{(110)}$  is 1.4 eV. The next two configurations are

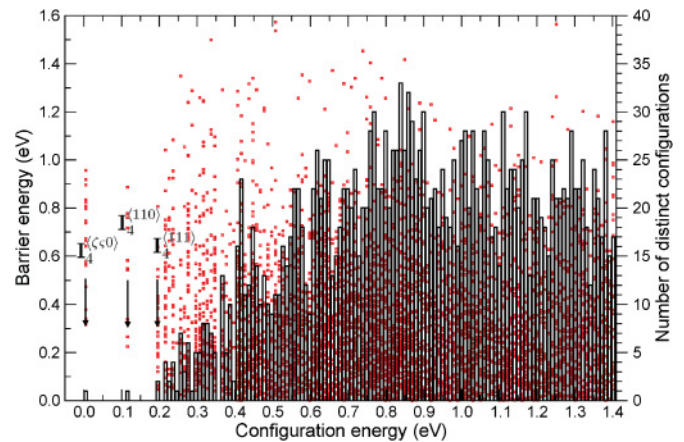


FIG. 9. (Color online) Histogram of the local minimum configurations and their respective barrier energies for  $I_4$ . The configuration energies are taken with respect to the energy of most stable configuration. The same convention is applied as in Fig. 2.

obtained by on-site rotations of the dumbbells, respectively, to the  $\langle 110 \rangle$  and  $\langle 111 \rangle$  directions. The latter configuration, at 0.20 eV, is the beginning of the continuum of states.

As shown in Fig. 4, the lowest-energy saddle points are at 0.25, 0.28, 0.31, and 0.34 eV. The lowest one corresponds to a  $\langle 111 \rangle$  glide of  $I_4^{(111)}$  with an energy barrier of 50 meV. The second one is similar, but it involves configurations close to  $I_4^{(111)}$ . The third and fourth ones correspond to on-site reorientations of the dumbbells from the  $I_4^{(\zeta \zeta 0)}$  configuration to, respectively, a distinct  $I_4^{(\zeta \zeta 0)}$  configuration and a  $I_4^{(110)}$  configuration.

Anento *et al.*<sup>38</sup> and Terentyev *et al.*<sup>35</sup> MD analyses of the tetra-interstitial show well-defined 1D-3D motions in the range of 300–1000 K with long 1D-glide stretches, during which the cluster adopts mostly the  $\langle 111 \rangle$  orientation, interrupted by rare transformations into  $I_4^{(110)}$ , or more likely  $I_4^{(\zeta \zeta 0)}$ , according to the present results. These MD results are perfectly consistent with the ARTn energy landscape: (1) There is no low-energy mechanism for  $I_4^{(\zeta \zeta 0)}$  to migrate as a unit; (2) the energy barrier for the  $I_4^{(111)} \rightarrow I_4^{(\zeta \zeta 0)}$  on-site rotation is 0.16 eV, i.e., much larger than the migration energy of  $I_4^{(111)}$  (0.05 eV);  $I_4^{(111)}$  will therefore perform several jumps in the  $\langle 111 \rangle$  direction before returning to  $I_4^{(\zeta \zeta 0)}$  and then rotating to another  $\langle 111 \rangle$  direction (or the same direction). The low-temperature limit of the activation energy for diffusion in the present energy landscape is the saddle-point energy of the  $\langle 111 \rangle$  glide of  $I_4^{(111)}$ , i.e., 0.25 eV. It can be shown that the Arrhenius slope will decrease with increasing temperature. These results are consistent with the MD results of Anento *et al.*, which also show a decrease of the activation energy with increasing temperature and an

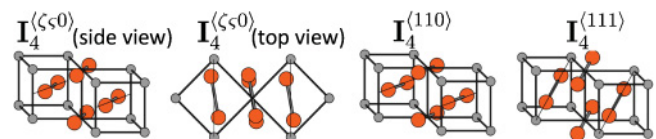


FIG. 10. (Color online) Schematic representation of the lowest-energy configurations of  $I_4$  (below the quasicontinuum).

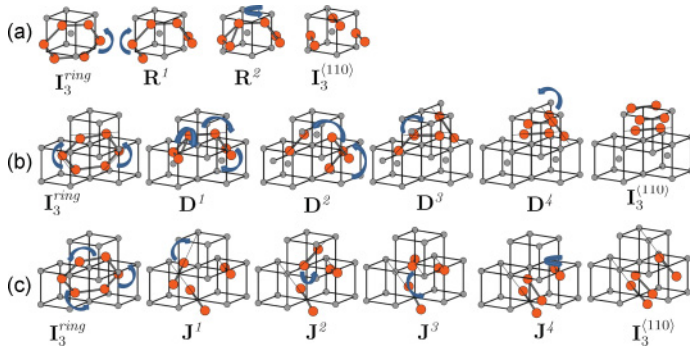


FIG. 11. (Color online) Unfaulting mechanisms of the tri-interstitial ring configuration,  $I_3^{\text{ring}}$ , into the  $I_3^{(110)}$  configuration: (a) 2 Johnson-rotation, (b) 2 Johnson-dissociation, and (c) 3 Johnson.

average value of 0.16 eV in the 300–500 K temperature range. Anento *et al.* also measured the rotation frequency between various  $\langle 111 \rangle$  directions. The corresponding activation energy is reported to be temperature dependent, but taking the average over the 300–900 K range, one obtains 0.36 eV. This value is in very good agreement with the present activation energy for the  $I_4^{\langle \zeta \zeta 0 \rangle} \rightarrow I_4^{\langle 111 \rangle}$  on-site rotation, i.e., 0.36 eV.

### E. Transition pathways

It is also possible to use ART $n$  coupled with the Metropolis algorithm for finding transition pathways<sup>47</sup> from high-energy configurations to lower-energy configurations. Recently, self-trapped configurations were proposed for the interstitial clusters:<sup>34</sup> for the  $I_2$ , the configuration  $I_2^{3b}$  seen in Fig. 3; for the tri-interstitial, the ring configuration  $I_3^{\text{ring}}$  made of three nonparallel  $\langle 110 \rangle$  dumbbells in a  $\langle 111 \rangle$  plane (see Fig. 11); and, in the  $I_4$  case, the ring configuration  $I_4^{\text{ring}}$ , obtained from  $I_3^{\text{ring}}$  by adding a  $\langle 111 \rangle$  dumbbell at the center of the ring. These configurations, being composed of nonparallel dumbbells, can be considered as *faulted* loops that cannot migrate by the simple step mechanism. The unfaulting energy barrier can be very large and in MD simulations the pathway is difficult to identify at high temperature, but too rare to observe at low temperature.<sup>34</sup> For example, the unfaulting activation energies are estimated at  $0.43 \pm 0.08$  and  $0.15 \pm 0.04$  eV for the  $I_2^{3b}$  and the  $I_3^{\text{ring}}$ , respectively, giving an average lifetime of less than 1 ns at 450 and 300 K, respectively, but increasing rapidly with falling  $T$ . The lifetime of the  $I_4^{\text{ring}}$  configuration is much longer—even in multiple ns MD simulations, this configuration often does not unfault—so the unfaulting activation energy is still a matter of debate, with an estimated value of  $1.68 \pm 0.3$  eV given by Terentyev *et al.*<sup>34</sup> and  $0.8 \pm 0.1$  eV given by Fan *et al.*<sup>11</sup>

At 0 K, the case of the  $I_2^{3b}$  configuration was already discussed in Sec. III B. This configuration lies in a flat

energy basin together with other configurations and can easily transform into the parallel configuration,  $I_2^{(110)}$  (see Fig. 5). The barrier of the mechanism  $I_2^{3b} \rightarrow I_2^{(110)}$  is 0.2 eV.

Performing ART $n$  simulations with different values of the fictitious Metropolis temperature, namely, 100, 400, and 800 K, we ensure a broader exploration of the different ways to escape from the starting minima. Hence, we are able to provide the complete path for the unfaulting mechanisms of the  $I_3^{\text{ring}}$  and  $I_4^{\text{ring}}$  into the parallel configurations  $I_3^{(110)}$  and  $I_4^{\langle \zeta \zeta 0 \rangle}$ , respectively. For each Metropolis temperature and each trapped configuration we performed  $10^3$  ART $n$  trajectories. Each trajectory is stopped once it reaches the desired configuration. In the random paths generated by ART $n$ , some configurations can be redundant and do not contribute to the net transition. Consequently, we illustrate only the lowest barrier energy paths and the shortest as the number of jumps. These successive jumps for  $I_3$  and  $I_4$  are presented in Figs. 11–13, respectively.

It is interesting to note that all the  $3 \times 10^3$  unfaulting mechanisms found by ART $n$  for  $I_3^{\text{ring}}$  begin with the same succession of two or three Johnson jumps. The shortest sequence starts with two successive Johnson jumps, followed by an on-site rotation of the dumbbell perpendicular to the other two. The intermediate configurations are labeled  $R^1$  and  $R^2$  to characterize this “2 Johnson + 1 rotation” sequence (see Figs. 11 and 12). The second sequence shown in Fig. 11 starts with the same two initial Johnson jumps, but the high-barrier energy on-site rotation is replaced by a sequence of Johnson jumps, the first three being simultaneous. The label D is used for the intermediate configurations, because the cluster looks almost dissociated. The third sequence starts with three simultaneous Johnson jumps, followed by a series of single Johnson jumps. The intermediate configurations are labeled J.

Energy profiles along the reaction coordinate of these three sequences are shown in Fig. 12. The most energetically

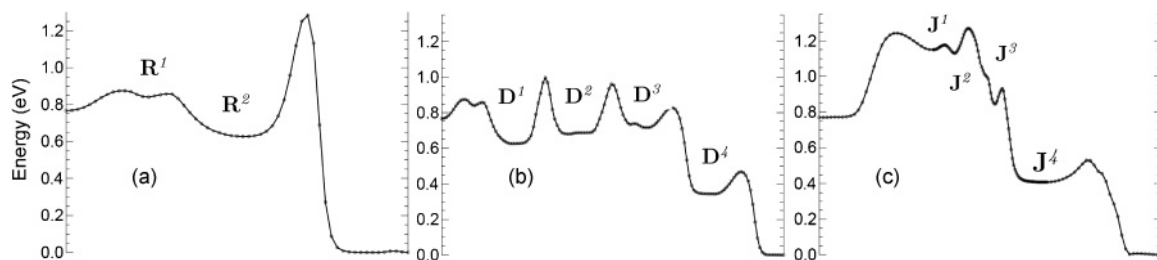


FIG. 12. Energy landscape for the three sequences of unfaulting mechanism of the tri-interstitial ring configuration,  $I_3^{\text{ring}}$ , into the  $I_3^{(110)}$  configuration shown in Fig. 11.

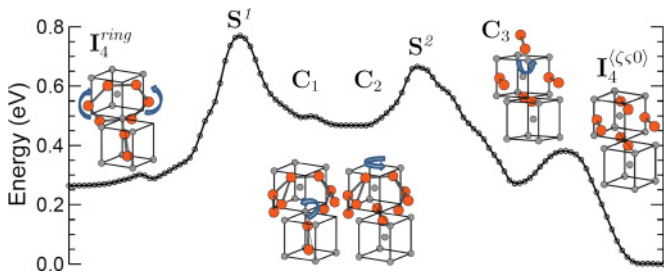


FIG. 13. (Color online) Transition pathway for the unfauling mechanism of the ring configuration of the tetrainterstitial,  $I_4^{\text{ring}}$ , into the most stable configuration,  $I_4^{(\zeta\zeta^0)}$ .

favorable is the 2 Johnson-dissociation mechanism: The difference between the highest saddle point—between  $D_1$  and  $D_2$ —and the initial configuration is 0.23 eV, but it corresponds to a barrier of 0.38 eV.

In the unfauling sequences starting from  $I_3^{\text{ring}}$ , we have observed (not shown) other pathways leading to the mobile configurations  $I_3^2$ ,  $I_3^3$ ,  $I_3^{(111)}$ , etc. All these trajectories start with the sequence  $I_3^{\text{ring}} \rightarrow D_1 \rightarrow D_2$  and have their highest saddle point between  $D_1$  and  $D_2$ .

The shortest and lowest-energy unfauling mechanism in the case of  $I_4^{\text{ring}}$  is presented in Fig. 13. It resembles the 2 Johnson-rotation sequence identified for the tri-interstitial. After the two first Johnson jumps, the  $\langle 111 \rangle$  dumbbell rotates into  $\langle 110 \rangle$ , and then the perpendicular dumbbell performs two jumps to realign to the other dumbbells. The highest barrier, which reaches 0.5 eV, occurs in the first part of the pathway, between  $I_4^{\text{ring}}$  and  $C_1$ . Using the autonomous basin climbing method, Fan *et al.*<sup>11</sup> found a path with a higher barrier, 0.86 eV.

The 0 K lowest unfauling energies of  $I_2^{3b}$ , 0.2 eV, and  $I_3^{\text{ring}}$ , 0.23 eV, are not far from the 300–550 K MD values,  $0.43 \pm 0.08$  and  $0.15 \pm 0.07$ , respectively. On the other hand, in the case of  $I_4^{\text{ring}}$ , the unfauling energy estimated here, from 0 K simulations, to be 0.5 eV, is significantly lower than the  $1.7 \pm 0.3$  eV deduced from the lifetime of the configuration obtained in MD simulations at 700–800 K by Terentyev *et al.*,<sup>34</sup> but it is quite close to the improved

value of  $0.8 \pm 0.1$  eV obtained by Fan *et al.*<sup>11</sup> using a broader temperature range, namely, 875–1050 K, and better statistics. The discrepancy between the present 0 K estimate and the latter high-temperature value probably arises, on the one hand, from anharmonic effects and, on the other hand, from the limitation in the fit to MD.<sup>48–50</sup>

The free-energy landscape of the unfauling mechanism of  $I_4^{\text{ring}}$  is expected to evolve with temperature because the initial configuration,  $I_4^{\text{ring}}$ , has a larger vibrational formation entropy than the final one,  $I_4^{(\zeta\zeta^0)}$ .<sup>34</sup> We have therefore determined the temperature dependence of the free-energy differences between the maxima  $S_{1,2}$  and the local minima  $C_{1,2,3}$  and  $I_4^{\text{ring}}$  using the transition-state theory in the harmonic approximation<sup>50,51</sup> at constant volume.<sup>40</sup>

The results, displayed in Fig. 14, show a striking difference between  $I_4^{\text{ring}}$  and  $C_{1,2,3}$ : Whereas the free-energy differences involving  $C_{1,2,3}$  decrease with temperature—indicating that the free-energy landscape becomes flatter with increasing temperature—it increases when the local minima is  $I_4^{\text{ring}}$ , leading to an increase of the unfauling free energy. Another interesting feature stems from the fact that  $S_1$  has a larger vibrational entropy than  $S_2$ . As a consequence, the saddle-point free energy of  $S_2$ , which is lower than that of  $S_1$  by 0.1 eV at 0 K, becomes actually higher above 320 K. More precisely, at 900 K, a temperature typical of the MD simulations of Refs. 11 and 34,  $\Delta F_{\text{vib}}^{I_4^{\text{ring}} \rightarrow S_1} = 0.41$  eV and  $\Delta F_{\text{vib}}^{I_4^{\text{ring}} \rightarrow S_2} = 0.71$  eV, giving free-energy differences with respect to  $I_4^{\text{ring}}$  of 0.91 and 1.11 eV for  $S_1$  and  $S_2$ , respectively.

These results demonstrate that there is a pronounced entropic effect along the transition pathway of the unfauling mechanism from  $I_4^{\text{ring}}$  to  $I_4^{(\zeta\zeta^0)}$ . This indicates that when performing kMC simulations on this type of energy landscape to deduce the mean time of the transformation from  $I_4^{\text{ring}}$  to  $I_4^{(\zeta\zeta^0)}$ , or  $I_4^{(111)}$  as in Ref. 11, one should take different prefactors for the jump frequencies between local minima. This may slightly affect the activation energy for the whole process. On the other hand, when considering the lifetime of the detrapping event only, as in Ref. 34, this harmonic entropic effect does not change the activation energy. More

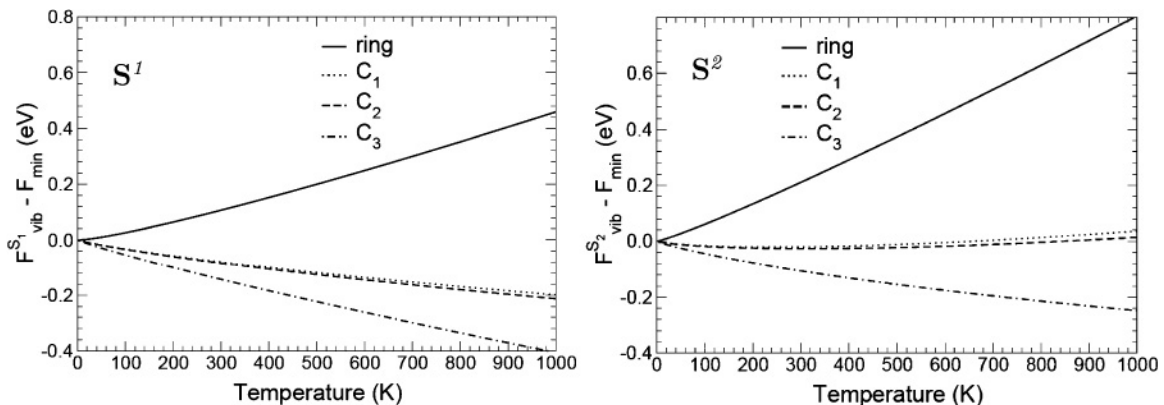


FIG. 14. Vibrational free-energy differences between the two highest saddle points,  $S_1$  (left-hand side) and  $S_2$  (right-hand side), and the intermediate-energy minima of the pathway for the unfauling mechanism of  $I_4^{\text{ring}} \rightarrow I_4^{(\zeta\zeta^0)}$  from Fig. 13.

sophisticated techniques should be used to investigate possible anharmonic effects.<sup>15,52,53</sup>

#### IV. CONCLUSION

A systematic study of the energy landscape of small interstitial clusters in iron modeled by the Ackland-Mendelev potential has been performed using the ART nouveau method.<sup>20,21</sup> We find that the number of bound configurations increases rapidly with cluster size, exceeding 400, 1100, and 1500 distinct bound configurations for  $I_2$ ,  $I_3$ , and  $I_4$ , respectively. These leads to the appearance of a quasicontinuous band of states at relatively low energy above the ground state—at 0.42, 0.23, and 0.20 eV for  $I_2$ ,  $I_3$ , and  $I_4$  respectively—with only a few isolated metastable configurations in between. Focusing on the states below the quasicontinuum, we identify all the low-energy configurations as well as the most relevant pathways that link them. For  $I$  and  $I_2$ , the lowest saddle-point energy migration mechanisms transform the lowest-energy configuration by a translation-rotation jump of the  $\langle 110 \rangle$  dumbbells. For  $I_3$  and  $I_4$ , migration is more complicated and takes place via a series of jumps between configurations with higher energies. Three such mechanisms are identified for  $I_3$ , including one that involves a configuration with  $\langle 110 \rangle$  and  $\langle 111 \rangle$  dumbbells, 0.29 eV above the lowest-energy configuration, which can glide easily in the  $\langle 111 \rangle$  direction.

The ARTn was also used to characterize the unfauling of the  $I_{3-4}^{\text{ring}}$  ring configurations. The results are in qualitative agreement with the brute-force MD calculations performed at higher temperature.<sup>11,34</sup> A different unfauling pathway, with a lower activation energy than in a previously proposed mechanism, namely, 0.5 eV, is obtained for  $I_4^{\text{ring}}$ . We find that the free energy of this barrier increases with the temperature owing to the large formation entropy of the  $I_4^{\text{ring}}$  configurations. The combination of ARTn with entropy calculations can thus provide a complete picture of the energy barrier evolution.

A detailed knowledge of the potential energy surface of point defects can be a valuable input for larger scale in space or time simulations.<sup>46,54</sup> The results of this paper open unique ways of studying the complex mechanisms responsible for defect diffusion using the ARTn method combined with good empirical potential and *ab initio* calculations.

#### APPENDIX A: GLOBAL VERSUS LOCAL DEFORMATION

This Appendix describes how the initial ARTn displacement direction, used in Eq. (1), can be chosen. It is defined by the  $\delta \mathbf{q}^i = (\delta \mathbf{q}_1^i, \delta \mathbf{q}_2^i, \dots, \delta \mathbf{q}_N^i)$  vector, where the  $j$ th component  $\delta \mathbf{q}_j^i = (q_{jx}^i, q_{jy}^i, q_{jz}^i)$  is a displacement applied to the  $j$ th atom of the crystal. We have tried two types of initial deformations: (i) a *global* deformation, where the random direction involves all the components of  $\delta \mathbf{q}^i$ ; and (ii) a *local, defect-centered* deformation, where the random deformation concerns only the atoms inside a sphere centered on the defect. Unless otherwise stated, a value of  $R_c = 6 \text{ \AA}$  is taken for the sphere radius for the monointerstitial test case.

The efficiency of the ARTn method for both types of deformations and several values of the  $\delta x_A$  displacement are presented in Table II for the case of the self-interstitial and a 1025-atom system. As a general trend, the total number of

TABLE II. Efficiency of the ARTn method tested in the case of a self-interstitial in Fe for two types of deformations and various displacement amplitudes,  $\delta x_A$ , expressed in  $\text{\AA}$ . For each case the statistics is made for a total of  $10^3$  successful trajectories.  $\eta_t$  is the trajectory efficiency, the number of successful trajectories over the total number of trajectories.  $\eta_f$  is the force efficiency, the number of force evaluations performed within the successful trajectories over the total number of force evaluations.  $n_f$  is the average total number of force evaluations over the number of successful trajectories. The force evaluations to check for connectivity between initial and final configurations are not included in  $\eta_f$  and  $n_f$ .  $n_m$  is the number of distinct minima.

$\delta x_A$	$\eta_t$	$\eta_f$	$n_f$	$n_m$
Global deformation				
0.05	0.77	0.78	3180	2
0.10	0.78	0.80	1744	3
0.20	0.78	0.79	1049	3
0.40	0.75	0.76	709	2
0.60	0.73	0.72	623	3
0.80	0.70	0.70	613	2
1.00	0.64	0.65	661	4
Defect-centered deformation				
0.05	0.71	0.78	1579	1
0.10	0.83	0.87	965	2
0.20	0.88	0.92	553	2
0.40	0.86	0.90	404	3
0.60	0.85	0.90	382	4
0.80	0.84	0.89	424	4
1.00	0.85	0.87	505	4

force evaluations per saddle point,  $n_f$ , increases when  $\delta x_A$  decreases, simply because more steps are needed to reach the saddle point when the amplitude of the steps decreases. In the case of global deformation and defect-centered deformation, the optimal value of  $\delta x_A$  is between 0.6 and 1.0  $\text{\AA}$ . The most efficient deformation is the defect-centered one: For  $\delta x_A = 0.6 \text{ \AA}$  only 400 force evaluations are needed as compared to twice as many in the case of global deformation. The superiority of the defect-centered deformation can be seen on three criteria listed in Table II: (1) the increase of the trajectory efficiency,  $\eta_t$ , defined as the number of successful trajectories over the total number of trajectories; (2) the increase of the force efficiency  $\eta_f$ , defined as the number of force evaluations performed within the successful trajectories over the total number of force evaluations; and (3) the overall larger number of distinct configurations found,  $n_m$ . Note that for  $n_m$  the parameter  $\delta x_A$  also matters: For both types of deformation, some configurations are not found after  $10^3$  activation events if  $\delta x_A$  is too small. For instance, the tetrahedral configuration is missing for  $\delta x_A < 0.6 \text{ \AA}$ .

The superiority of the local deformation can be interpreted in terms of the nature of the normal modes involved in the activation process. The local deformation excites preferentially the local phonons, whereas the global deformation excites both local and delocalized modes. Delocalized modes or long-wavelength phonons will induce only global displacements. Following a delocalized mode deformation, ARTn needs many

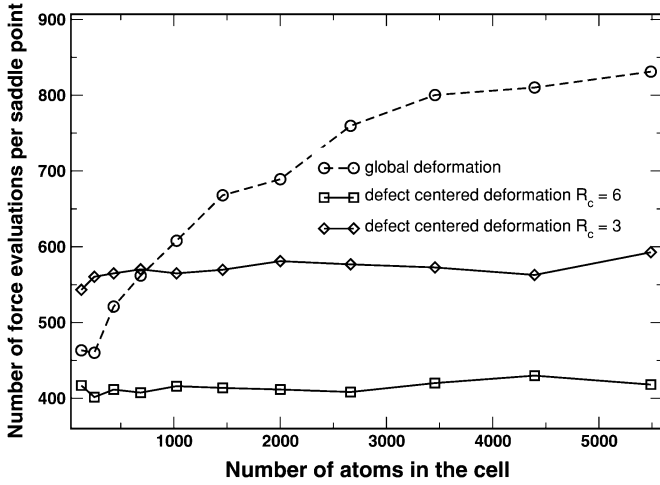


FIG. 15. Dependence with system size of the efficiency of the ARTn method: Comparison between the global deformation and the defect-centered deformation with two different deformation-sphere radii.

steps to escape from the harmonic basin and therefore many of these events are rejected. The superiority of the local deformation shows that the displacement toward the saddle point is mostly composed of local normal modes.

The most important improvement of the defect-centered deformation over the global deformation is seen in the dependence with system size of the number of force evaluations per saddle point,  $n_f$ , for a constant number of defects (i.e., a linear decrease in defect density). The number of force evaluations in global moves is independent of system size, for example, in amorphous materials. Here, for the global deformation,  $n_f$  increases continuously with the number of atoms in the system. On the other hand, for the defect-centered deformation  $n_f$  is almost constant from 129 atoms ( $4a_0 \times 4a_0 \times 4a_0$  cell) to 5489 atoms ( $14a_0 \times 14a_0 \times 14a_0$  cell) (see Fig. 15). Note, however, that  $n_f$  is not an increasing function of the number of atoms that are implied in the deformation:  $n_f$  is indeed larger for  $R_c = 3 \text{ \AA}$  than for  $R_c = 6 \text{ \AA}$  (see Fig. 15). This reflects the fact that the normal modes involved in the activation process have significant components outside the sphere  $R_c = 3 \text{ \AA}$ .

In a study on surface adatom diffusion Pt/Pt(111) using the dimer and ARTn methods,<sup>17</sup> Olsen *et al.* also showed that  $n_f$  increases with the number of atoms in the system, in agreement with our result for the global deformation. Furthermore, they reported that the number of distinct minima,  $n_m$ , depends on  $\delta x_A$ . They mention that for small values of  $\delta x_A$  the system can be trapped in bottlenecks and some saddle points are never reached. In our system of crystal defects, there is no obvious correlation between  $n_m$  and  $\delta x_A$ . This correlation is observed only in the case of local deformation.

## APPENDIX B: LANCZOS METHOD IN ARTn

Let  $\mathbf{H}[\mathbf{q}_0]$  be the Hessian matrix of the system at the phase-space point  $\mathbf{q}_0$ :

$$H_{i\alpha,j\beta}[\mathbf{q}_0] = \frac{\partial^2 E[\mathbf{q}_0]}{\partial q_{i\alpha} \partial q_{j\beta}}, \quad (\text{B1})$$

where  $E[\mathbf{q}_0]$  is the energy of the system at point  $\mathbf{q}_0$ .  $\mathbf{H}$  is a real and symmetric matrix. For ARTn we need only the lowest eigenvalue,  $\lambda_1$ , and its eigenvector,  $\mathbf{v}_1$ . The Lanczos algorithm is an efficient way to extract a limited spectrum of eigenvalues and eigenvectors and it does not require evaluating the full  $3N \times 3N$  matrix  $\mathbf{H}$ . The diagonalization of the full Hessian matrix is replaced by that of a  $l \times l$  trigonal matrix ( $l \ll 3N$ ), and the  $\mathbf{H}$  matrix needs to be known only in the  $l$ -dimensional space of the Lanczos vectors.

In the following we describe how the Lanczos scheme is used to calculate  $\lambda_1$  and  $\mathbf{v}_1$ . First of all, we must build the Lanczos basis in which the  $\mathbf{H}$  matrix is trigonal. Consider  $\mathbf{u}_0$  a *random* normalized vector in  $\mathbf{R}^{3N}$  space. The result of the application of  $\mathbf{H}$  on  $\mathbf{u}_0$  can be decomposed as a linear combination of this random vector and a second normalized one,  $\mathbf{u}_1$ , orthogonal to  $\mathbf{u}_0$ :

$$\mathbf{H}\mathbf{u}_0 = a_0\mathbf{u}_0 + b_1\mathbf{u}_1. \quad (\text{B2})$$

The application of the Hessian on  $\mathbf{u}_1$  becomes

$$\mathbf{H}\mathbf{u}_1 = a_1\mathbf{u}_1 + b'_1\mathbf{u}_0 + b_2\mathbf{u}_2, \quad (\text{B3})$$

where  $\mathbf{u}_2$  is a normalized vector that is orthogonal to the first two. Because  $\mathbf{H}$  is a symmetric matrix,

$$\mathbf{u}_1 \cdot (\mathbf{H}\mathbf{u}_0) = \mathbf{u}_0 \cdot (\mathbf{H}\mathbf{u}_1), \quad (\text{B4})$$

and therefore  $b_1 = b'_1$ . The full recursion scheme becomes

$$\mathbf{H}\mathbf{u}_k = a_k\mathbf{u}_k + b_k\mathbf{u}_{k-1} + b_{k+1}\mathbf{u}_{k+1} \quad (\text{B5})$$

for  $0 < k < l - 1$  and the closure of the recursion for  $k = l - 1$ :

$$\mathbf{H}\mathbf{u}_{l-1} = a_{l-1}\mathbf{u}_{l-1} + b_{l-1}\mathbf{u}_{l-2}. \quad (\text{B6})$$

In this  $l$ -dimensional basis  $(\mathbf{u}_0, \mathbf{u}_1, \dots, \mathbf{u}_{l-1})$  the  $\mathbf{H}$  matrix is trigonal:

$$\mathbf{T}_l = \begin{pmatrix} a_0 & b_1 & 0 & \cdots & 0 \\ b_1 & a_1 & b_2 & \cdots & 0 \\ 0 & b_2 & a_2 & \cdots & 0 \\ 0 & \ddots & \ddots & \cdots & 0 \\ 0 & & b_{l-2} & a_{l-2} & b_{l-1} \\ 0 & & 0 & b_{l-1} & a_{l-1} \end{pmatrix}. \quad (\text{B7})$$

The central point of the Lanczos method is that it can be demonstrated that the lowest eigenvalue of the  $\mathbf{H}$  matrix,  $\lambda_1[\mathbf{H}]$ , is the limit of the series  $\lambda_1[\mathbf{T}_l]$  with  $l \rightarrow 3N$ . Finally, the eigenvector  $\mathbf{v}_1[\mathbf{H}]$  corresponding to the lowest eigenvalue  $\lambda_1[\mathbf{H}]$  can be approximated by the eigenvector associated with the lowest eigenvalue of the  $\mathbf{T}_l$ ,  $\mathbf{v}_1[\mathbf{T}_l]$ .

The vectors  $\mathbf{H}[\mathbf{q}_0]\mathbf{u}$  can be calculated by the finite difference on the forces by performing a Taylor expansion of the forces around  $\mathbf{q}_0 + \delta_L\mathbf{u}$  ( $\delta_L \ll 1$ ), a point in the neighborhood of  $\mathbf{q}_0$  in the direction  $\mathbf{u}$ :

$$\mathbf{H}[\mathbf{q}_0]\mathbf{u} = -\frac{\mathbf{f}(\mathbf{q}_0 + \delta_L\mathbf{u}) - \mathbf{f}(\mathbf{q}_0)}{\delta_L} + O(\delta_L^2). \quad (\text{B8})$$

This expansion can also be made,  $O(\delta_L^3)$ :

$$\mathbf{H}[\mathbf{q}_0]\mathbf{u} = -\frac{\mathbf{f}(\mathbf{q}_0 + \delta_L\mathbf{u}) - \mathbf{f}(\mathbf{q}_0 - \delta_L\mathbf{u})}{2\delta_L} + O(\delta_L^3). \quad (\text{B9})$$

It is important to note that using this  $O(\delta_L^3)$  approximation requires two times as many force evaluations than Eq. (B8): Both  $\mathbf{f}(\mathbf{q}_0 + \delta_L \mathbf{u})$  and  $\mathbf{f}(\mathbf{q}_0 - \delta_L \mathbf{u})$  must be evaluated compared to only  $\mathbf{f}(\mathbf{q}_0 + \delta_L \mathbf{u})$  in the case of Eq. (B8), because  $\mathbf{f}(\mathbf{q}_0)$  is computed anyway at every step for the minimization in the hyperplane orthogonal to  $\mathbf{v}_1$  and for the test of convergence to the saddle point.

The parameters that must be optimized for the calculation of the Lanczos coefficients ( $a_k, b_k$ ) and vectors  $\mathbf{u}_k$  from Eqs. (B2), (B5), and (B6) are the size of the Lanczos basis set,  $l$ , and the step of the numerical derivative of forces for the Hessian,  $\delta_L$ . In this paper we have used  $l = 15$  and  $\delta_L = 10^{-3}$  Å with an  $O(\delta_L^2)$  expansion. This choice results from an analysis performed on a test system with 1025 atoms (one self-interstitial defect in a  $8a_0 \times 8a_0 \times 8a_0$  bcc cell). A random deformation is applied to the minimum energy configuration ( $\langle 110 \rangle$  orientation of the dumbbell) in order to induce an imaginary frequency. Taking  $l = 15$ , we have calculated  $\lambda_1$  using an expansion of order either 2 [Eq. (B8)] or 3 [Eq. (B9)], and three different values of  $\delta_L = 10^{-2}$ ,  $10^{-3}$ , and  $10^{-4}$  Å. The numerical stability of the algorithm is tested by performing an iterative Lanczos diagonalization. Successive iterations of  $l$  Lanczos steps are performed, where each new iteration,  $i$ , is started by taking for  $u_0$  the last vector of the Lanczos basis set,  $u_{l-1}$ , of the previous Lanczos iteration,  $i - 1$ . As illustrated in Fig. 16, in both cases  $\delta_L = 10^{-4}$  Å shows numerical instabilities as functions of the number of Lanczos iterations, in particular, for the order 2 expansion. For  $\delta_L = 10^{-2}$  Å some numerical noise appears only in the case of  $O(\delta_L^2)$  force derivatives. But for  $\delta_L = 10^{-3}$  Å the same accuracy is obtained in both cases. In conclusion, the maximum efficiency can be obtained using Eq. (B8) and  $\delta_L = 10^{-3}$  Å.

In a method such as ARTn, where successive Hessian matrices of systems that differ by only small displacements must be evaluated, the efficiency of the Lanczos method can be considerably improved by optimizing the choice of the first vector,  $u_0$  in Eq. (B2). As for an iterative diagonalization, the idea is to take for  $u_0$  at every ARTn step,  $i$ , the last vector of

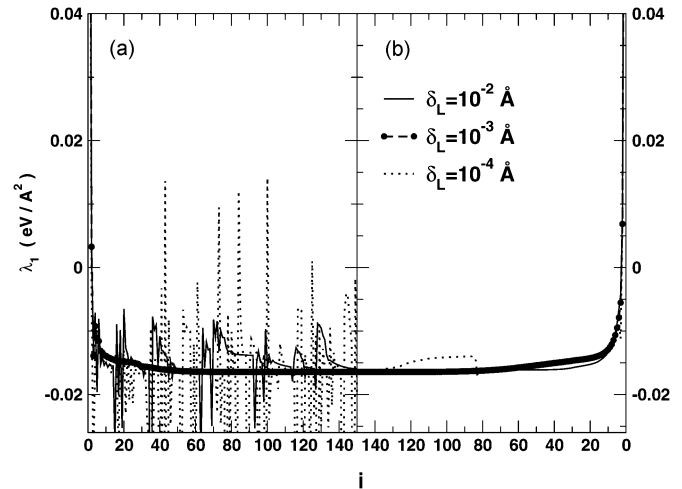


FIG. 16. Convergence as a function of the number of Lanczos iterations of the smallest eigenvalue of the Hessian,  $\lambda_1$ , for a system with 1025 iron atoms using a Lanczos basis of size  $l = 15$ . The Hessian is computed using (a) order 2 derivatives as in Eq. (B8) or (b) order 3 derivatives as in Eq. (B9).

the Lanczos basis set,  $u_{l-1}$ , of the previous ARTn step,  $i - 1$ . If the displacements between ARTn steps are small, the convergence with the size of the Lanczos basis,  $l$ , after  $i$  ARTn steps is close to that of a basis set of size  $i \times l$  using a random  $u_0$  vector. The convergence with the size of the Lanczos basis set is therefore not a problem. In practice,  $l = 15$  provides a good accuracy after  $i \sim 4$  ARTn steps and excellent accuracy after 20 steps, as illustrated in Fig. 16. Another proof of the good convergence with respect to  $l$  can be seen from the fact that the discrepancy between the Lanczos and NEB values of the barrier energies of the self-interstitial summarized in the Table I are less than 0.01 eV, even when the system size increases from 129 to 1025 atoms. Indeed, the error in the estimation of the lowest eigenvalue varies as  $N/(l \times i)$ .

<sup>1</sup>I. Cook, *Nat. Mater.* **5**, 77 (2006).

<sup>2</sup>A. F. Voter, *J. Chem. Phys.* **106**, 4665 (1997).

<sup>3</sup>A. F. Voter, *Phys. Rev. B* **57**, R13985 (1998).

<sup>4</sup>M. R. Sorensen and A. F. Voter, *J. Chem. Phys.* **112**, 9599 (2000).

<sup>5</sup>D. Passerone and M. Parrinello, *Phys. Rev. Lett.* **87**, 108302 (2001).

<sup>6</sup>D. Passerone, M. Ceccarelli, and M. Parrinello, *J. Chem. Phys.* **118**, 2025 (2003).

<sup>7</sup>H. Vocks, M. V. Chubynsky, G. T. Barkema, and N. Mousseau, *J. Chem. Phys.* **123**, 244707 (2005).

<sup>8</sup>B. P. Uberuaga, R. Smith, A. R. Cleave, F. Montalenti, G. Henkelman, R. W. Grimes, A. F. Voter, and K. E. Sickafus, *Phys. Rev. Lett.* **92**, 115505 (2004).

<sup>9</sup>B. P. Uberuaga, R. G. Hoagland, A. F. Voter, and S. M. Valone, *Phys. Rev. Lett.* **99**, 135501 (2007).

<sup>10</sup>X.-M. Bai, A. F. Voter, R. G. Hoagland, M. Nastasi, and B. P. Uberuaga, *Science* **327**, 1631 (2010).

<sup>11</sup>Y. Fan, A. Kushima, and B. Yildiz, *Phys. Rev. B* **81**, 104102 (2010).

<sup>12</sup>H. Jonsson, *Annu. Rev. Phys. Chem.* **51**, 623 (2000).

<sup>13</sup>G. Henkelman and H. Jonsson, *J. Chem. Phys.* **113**, 9978 (2000).

<sup>14</sup>G. Henkelman, G. Johansson, and H. Jonsson, in *Progress in Theoretical Chemistry and Physics* (Kluwer, Academic, 2000).

<sup>15</sup>D. J. Wales, *Energy Landscapes* (Cambridge University Press, Cambridge, UK, 2003).

<sup>16</sup>C. J. Cerjan and W. H. Miller, *J. Chem. Phys.* **75**, 2800 (1981).

<sup>17</sup>R. A. Olsen, G. J. Kroes, G. Henkelman, A. Arnaldsson, and H. Jonsson, *J. Chem. Phys.* **121**, 9776 (2004).

<sup>18</sup>A. Heyden, A. T. Bell, and F. J. Keil, *J. Chem. Phys.* **123**, 224101 (2005).

<sup>19</sup>G. T. Barkema and N. Mousseau, *Phys. Rev. Lett.* **77**, 4358 (1996).

<sup>20</sup>R. Malek and N. Mousseau, *Phys. Rev. E* **62**, 7723 (2000).

<sup>21</sup>N. Mousseau and G. T. Barkema, *Phys. Rev. B* **61**, 1898 (2000).

<sup>22</sup>N. Mousseau and G. T. Barkema, *Phys. Rev. E* **57**, 2419 (1998).

<sup>23</sup>G. Henkelman and H. Jonsson, *J. Chem. Phys.* **111**, 7010 (1999).

<sup>24</sup>L. J. Munro and D. J. Wales, *Phys. Rev. B* **59**, 3969 (1999).

<sup>25</sup>K. H. Robrock, P. Ehrhart, and H. R. Schober, in *Physics of Radiation Effects in Crystals* (Elsevier, Amsterdam, 1986).

- <sup>26</sup>C. Domain and C. S. Becquart, *Phys. Rev. B* **65**, 024103 (2001).
- <sup>27</sup>C. C. Fu, F. Willaime, and P. Ordejon, *Phys. Rev. Lett.* **92**, 175503 (2004).
- <sup>28</sup>F. Willaime, C.-C. Fu, M.-C. Marinica, and J. Dalla Torre, *Nucl. Instrum. Methods Phys. Res. Sect. B* **228**, 92 (2004).
- <sup>29</sup>P. M. Derlet, D. Nguyen-Manh, and S. L. Dudarev, *Phys. Rev. B* **76**, 054107 (2007).
- <sup>30</sup>B. C. Masters, *Nature (London)* **200**, 254 (1963).
- <sup>31</sup>B. L. Eyre and R. Bullough, *Philos. Mag.* **12**, 31 (1965).
- <sup>32</sup>A. E. Ward and S. B. Fischer, *J. Nucl. Mater.* **166**, 227 (1989).
- <sup>33</sup>J. Marian, B. D. Wirth, and J. M. Perlado, *Phys. Rev. Lett.* **88**, 255507 (2002).
- <sup>34</sup>D. A. Terentyev, T. P. C. Klaver, P. Olsson, M.-C. Marinica, F. Willaime, C. Domain, and L. Malerba, *Phys. Rev. Lett.* **100**, 145503 (2008).
- <sup>35</sup>D. A. Terentyev, L. Malerba, and M. Hou, *Phys. Rev. B* **75**, 104108 (2007).
- <sup>36</sup>S. L. Dudarev, R. Bullough, and P. M. Derlet, *Phys. Rev. Lett.* **100**, 135503 (2008).
- <sup>37</sup>Y. Abe and S. Jitsukawa, *Philos. Mag.* **89**, 375 (2009).
- <sup>38</sup>N. Anento, A. Serra, and Yu. N. Osetsky, *Modell. Simul. Mater. Sci. Eng.* **80**, 025008 (2010).
- <sup>39</sup>S. Takaki, J. Fuss, H. Kugler, U. Dedek, and H. Schultz, *Radiat. Eff.* **79**, 87 (1983).
- <sup>40</sup>M.-C. Marinica and F. Willaime, *Solid State Phenom.* **129**, 67 (2007).
- <sup>41</sup>G. J. Ackland, M. I. Mendelev, D. J. Srolovitz, S. Han, and A. V. Barashev, *J. Phys. Condens. Matter* **16**, S2629 (2004).
- <sup>42</sup>M. I. Mendelev, S. Han, D. J. Srolovitz, G. J. Ackland, D. Y. Sun, and M. Asta, *Philos. Mag.* **83**, 3977 (2003).
- <sup>43</sup>E. Cances, F. Legoll, M.-C. Marinica, K. Minoukadeh, and F. Willaime, *J. Chem. Phys.* **130**, 114711 (2009).
- <sup>44</sup>R. A. Johnson, *Phys. Rev.* **134**, A1329 (1964).
- <sup>45</sup>F. Gao, D. J. Bacon, Yu. N. Osetsky, P. E. J. Flewitt, and T. A. Lewis, *J. Nucl. Mater.* **276**, 213 (2000).
- <sup>46</sup>C.-C. Fu, J. Dalla Torre, F. Willaime, J.-L. Bocquet, and A. Barbu, *Nat. Mater.* **4**, 68 (2005).
- <sup>47</sup>G.-H. Wei, N. Mousseau, and P. Derreumaux, *J. Chem. Phys.* **117**, 11379 (2002).
- <sup>48</sup>G. Boisvert, L. J. Lewis, and A. Yelon, *Phys. Rev. Lett.* **75**, 469 (1995).
- <sup>49</sup>G. Boisvert, N. Mousseau, and L. J. Lewis, *Phys. Rev. B* **58**, 12667 (1998).
- <sup>50</sup>M.-C. Marinica, C. Barreteau, D. Spanjaard, and M.-C. Desjonqueres, *Phys. Rev. B* **72**, 115402 (2005).
- <sup>51</sup>P. Hännig, P. Talkner, and M. Borovec, *Rev. Mod. Phys.* **62**, 251 (1990).
- <sup>52</sup>S. Chiesa, P. M. Derlet, and S. L. Dudarev, *Phys. Rev. B* **79**, 214109 (2009).
- <sup>53</sup>M. Athenes and M.-C. Marinica, *J. Comp. Phys.* **229**, 7129 (2010).
- <sup>54</sup>T. Opplestrup, V. V. Bulatov, G. H. Gilmer, M. H. Kalos, and B. Sadigh, *Phys. Rev. Lett.* **97**, 230602 (2006).